Hindawi
Advances in Civil Engineering
Volume 2021, Article ID 3323434, 16 pages
https://doi.org/10.1155/2021/3323434

Research Article

Optimization of 110 m Aperture Fully Steerable Radio Telescope Prestressed Back Frame Structure Based on a Genetic Algorithm

Ge Gao,[1] **Kai Zhang**,[2] **and Shiru Sun**[2]

[1]*School of Business Administration, Liaoning Technical University, Huludao 125105, China*
[2]*School of Ocean Engineering, Harbin Institute of Technology at Weihai, Weihai 264209, China*

Correspondence should be addressed to Kai Zhang; zhangkai_hit@126.com

Received 19 May 2021; Accepted 25 August 2021; Published 6 September 2021

Academic Editor: Giovanni Garcea

Radio telescopes play an important role in lunar exploration projects, manned space flight projects, and navigation systems. China is constructing a giant 110 m aperture ground-based fully steerable radio telescope in Qitai County, Xinjiang Uygur Autonomous Region. In this paper, a 110 m aperture fully steerable radio telescope prestressed back frame structure is proposed and optimized to improve the reflector accuracy and to reduce the weight of the telescope. First, prestressed cables are introduced into the back frame structure, and three innovative cable layout schemes are presented. Second, for stress state analysis, the wind pressure distribution on the main reflector is explored using wind tunnel experiments. Third, some improvements in genetic algorithms for addressing computational complexity are explained. Finally, the effects of prestressed cables on the weight reduction and reflector accuracy improvement are analysed. Additionally, in order to evaluate the safety of the prestressed back frame structure, its strength has been checked, and the internal force and displacement under static conditions and in earthquakes are interpreted in detail.

1. Introduction

Large-aperture radio telescopes are greatly significant for the development of radio astronomy and space exploration [1–3]. To distinguish signals from cosmic radio sources, it is crucial for radio telescopes to have high sensitivity and resolution. Sensitivity refers to the ability of a radio telescope to detect weak signal sources, and resolution refers to its ability to distinguish nearby sources. In order to improve sensitivity and resolution of a telescope, the most widely used method is to expand its aperture. Therefore, large-aperture radio telescopes have been built around the world, with the intention of advancing deep space exploration. Among them, five hundred-meter aperture spherical radio telescope (FAST) [4, 5], located in Guizhou, China (Figure 1(a)), is the largest single aperture radio telescope in the world at present. The largest fully steerable radio telescopes are the Effelsberg 100 m telescope in Germany (Figure 1(b)) and the Green Bank 110 × 100 m telescope in America (GBT) (Figure 1(c)) [6]. The Chinese Academy of Sciences, National Development and Reform Commission, and the Xinjiang Uygur Autonomous Region are constructing a fully steerable radio telescope with a 110 m aperture, in Qitai County (QTT) [7]. When completed, it will be the largest fully steerable radio telescope in the world.

At present, the existing radio telescopes are mainly space trusses. The Effelsberg telescope was built in 1972. Its main structure represents the most common type of telescope structure [8]: it is assembled by a number of minimum units around the central axis, so that the telescope shows polar symmetry and its internal force is more uniform. When designing the GBT, deviation support scheme is adopted for the subreflector [9]: a 91 m giant extender truss is stretched out from the side of the pitching device to support the subreflector. Thus, the subreflector does not obstruct the main reflector but at the cost of a heavy structure, weighing 7300 t.

After decades of development, the optimization design concept for large-aperture radio telescope structures has become more mature [10–13]. In 1967, von Hoerner [14]

(a) (b) (c)

Figure 1: Radio telescopes around the world: (a) China: FAST; (b) Germany: Effelsberg; (c) America: GBT.

proposed the concept of homogeneous design. The main idea of this concept is to optimize the cross section of the back frame structure so that the reflector can maintain a new paraboloid under the action of gravity. The most famous application is the Effelsberg telescope, which has a reflector fitting accuracy of 0.5 mm, but the computation requirements, especially iterations, will increase exponentially with the increase in design variables. Afterwards, Chen and Ye [15] conducted an in-depth study and proposed a strict homogeneous design. The essence of this concept is to obtain the displacement difference between the reflector's nodes and the homogeneous surface through the initial analysis, establish some hypothetical displacement relationships, and finally make the deformation of the telescope meet the displacement using optimization design. However, this method still cannot be applied in practice because if the structure has N nodes, $3N$ constraints will significantly exceed the design variables, resulting in no solution for equations. Subsequently, Levy and Melosh [16] presented the criteria for optimizing the telescope design and demonstrated the feasibility of this method. Nevertheless, because the theoretical basis is not too firm, the iterative process is not stable enough, and different criterions need to be derived for different problems, this method is not widely used. In general, for structural design of telescopes, some researchers pursued high accuracy, resulting in a number of structural defects, while some aimed for simple structures, causing low accuracy.

To design a telescope structure, it is not enough to only choose a design concept. In fact, with the help of scientific algorithms, the geometries of the specific components can also be determined [17–19]. At present, structural optimization algorithms are mainly divided into analytical methods, optimality criteria methods, and mathematical programming methods. Traditional analytical methods and optimality criteria methods are less effective with an increase in the reflector aperture and increasing variables. Therefore, it is necessary to seek more convenient and efficient algorithms that can deal with a large number of variables. The genetic algorithm (GA), which is a mathematical programming method, can solve such problems well [20–23]. Currently, GAs have been widely used in structure optimization design. Goldberg and Samtani [24] and Rajeev and Krishnamoorthy [25] have used GAs to optimize truss structures. Adeli and Cheng [26] integrated GAs with a penalty function to study the optimization of spatial structures. Prendes Gero et al. [27, 28] presented an elitist GA and used it in structural optimization of two-dimensional trusses and three-dimensional steel space frames. Stanković et al. [29] introduced NSGA-II into GAs for synthesis of truss structure designs. Kociecki and Adeli [30] introduced a two-phase GA approach for minimum weight design of free-form steel space-frame roof structures. Grygierek [31] employed a self-adaptive approach based on fuzzy logic mechanism in GAs for the optimization of the weight of steel truss structures. Assimi and Jamali [32] coupled GAs and Nelder–Mead to conduct topology and size optimization of trusses with static and dynamic constraints. Delyová et al. [33] proposed a GA optimization program considering an additional bit for each bar. Villalba-Morales and Ramirez-Echeverry [34] optimized steel trusses by using a multichromosome GA with self-adaptive parameters.

In this paper, the research object is the 110 m aperture fully steerable radio telescope prestressed back frame structure, and the optimization design is conducted to reduce the weight and improve the reflector accuracy. First, a new scheme is proposed for applying prestressed cables to the back frame structure. Second, wind tunnel experiments are employed to investigate the wind pressure distribution on the reflector. Third, the improved GA techniques are expounded. Finally, the effects that prestressed cables have on reducing the weight and improving the reflector accuracy are analysed, and the structural safety is evaluated.

2. Design Scheme of the Prestressed Back Frame Structure

2.1. Innovative Prestressed Back Frame Structure. The fully steerable radio telescope is generally composed of a main reflector and a back frame structure, a subreflector and its supporting structure, a pitching device, and an azimuth mount. The overall model of the radio telescope is shown in Figure 2.

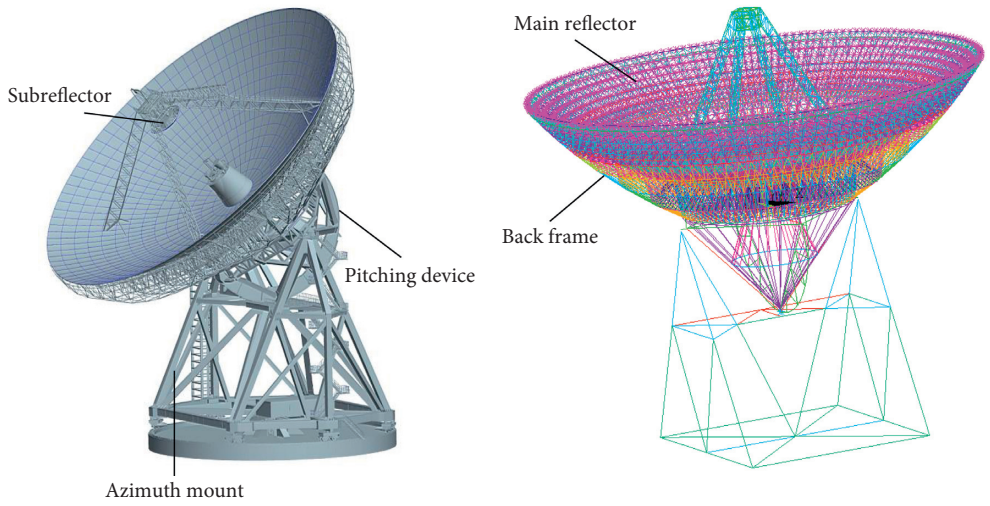

Figure 2: Model of QTT: (a) conceptual model; (b) numerical model.

(1) The main reflector is composed of an aluminium honeycomb panel and a number of actuators. It is connected to the top of the back frame. The reflector accuracy is ensured by changing the length of actuators. The main function of the back frame is to support the main reflector and maintain its geometric surface, which is essential in structural design. Usually, the space truss system is used in the back frame.

(2) The subreflector is an aluminium honeycomb sandwich structure, and its geometric surface is hyperboloid of revolution. It is supported on the main reflector by four steel trusses.

(3) The pitching device, which directly supports the back frame, consists of polygonal frame beams. In order to improve the reflector accuracy and ensure the uniform deformation of back frame, the pitching device is commonly designed to be polar symmetric.

(4) The azimuth mount is rotated by driving wheels in the horizontal plane around the pivot to complete the azimuth change.

As shown in Figure 3, the traditional back frame structure mainly consists of three types of rods, namely, circumferential rods, radial rods, and rigid web members. Web members connect the upper and lower rods to transmit the tensile pressure, and radial rods are connected via web members and provide bending stiffness. The main function of circumferential rods is to limit the out-of-plane deformation of the radial rods.

Prestressed structures are widely used in construction engineering. Compared with non-prestressed structures, prestressed structures are more efficient, economical, and energy-saving [35–37]. Since prestressed cables can increase the stiffness when applied to the monolithic tensioned structures, they are generally used in space deployable antennas [38, 39]. Previous studies have not used prestressed cables in fully steerable telescope structures, but prestressed cables are an effective method to reduce the weight of a structure. Therefore, this study suggests replacement of some specific robs by prestressed cables. Three prestressed cable layout schemes are proposed (Figure 4) as follows:

(1) *Scheme 1*. All robs in the 1st lap are replaced by prestressed cables

(2) *Scheme 2*. All robs in the 1st and 2nd laps are replaced by prestressed cables

(3) *Scheme 3*. All robs in the 1st, 2nd, and 3rd laps are replaced by prestressed cables

Rigid rods and circumferential cables compose the innovative prestressed back frame structural system. Certain initial prestress is first applied to the lower circumferential cables, and the middle rigid web members are used to support the upper reflector rods. The prestressed cables can improve the stress distribution of the telescope during normal operation and reduce the uneven deformation of the reflector so that the performance of each rod can be effectively exerted. Also, the internal force of prestressed cables is always tension in work, and thus the instability problem is avoided. Further, using prestressed cables can significantly reduce the overall steel consumption and cost.

2.2. Stress State Analysis of the Prestressed Back Frame Structure. From construction to normal operation, the stress states of the back frame structure can be divided into three stages: the zero state, prestressed state, and loading state. The zero state refers to the initial state of robs and cables prior to their installation. The prestressed state is the state in which the structure is installed after the cables are tensioned. The external load includes the structure weight, the reflector panel weight, and wind load. The loading state is the equilibrium state after structural deformation under the action of the external load.

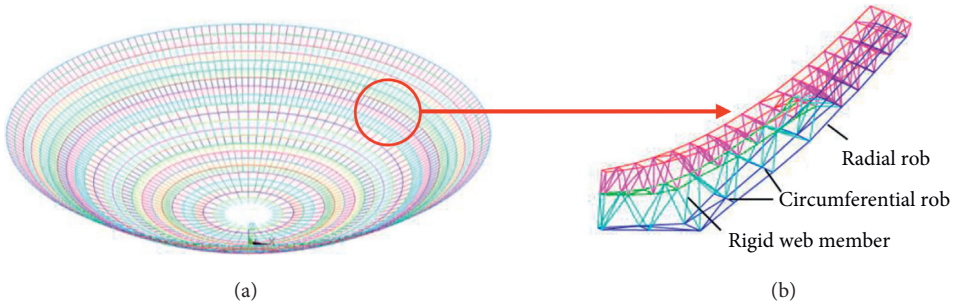

Figure 3: Back frame structure: (a) global view; (b) details of the back frame.

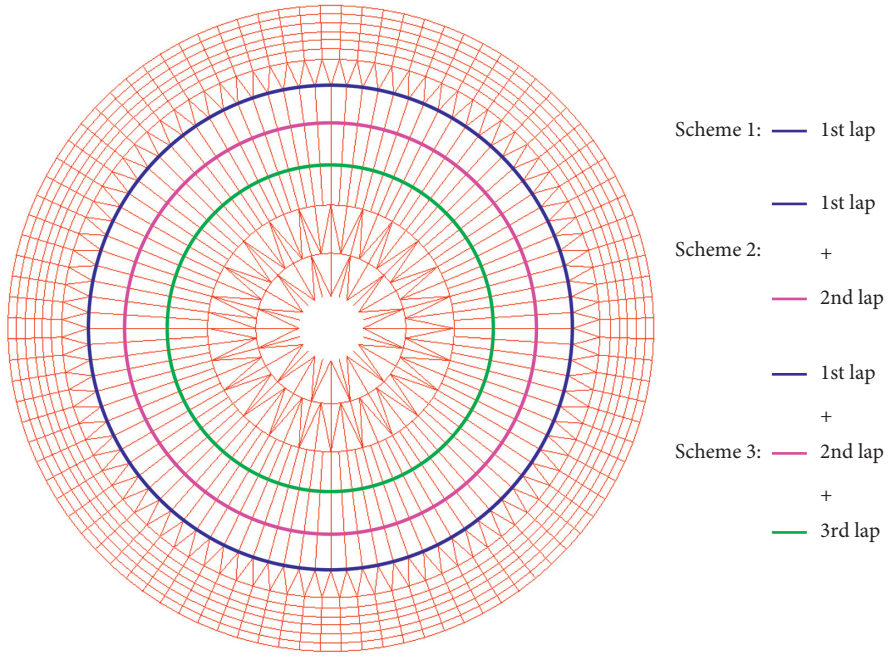

Figure 4: Innovative prestressed back frame structure.

When studying the stress states of the back frame structure, three test conditions, P_1, P_2, and P_3, are selected for the weight according to the pitch angles 5°, 30°, and 60°. Furthermore, three test conditions W_1, W_2, and W_3 are selected for the wind load according to the wind angle 0°, 90°, and 180°. The load case combinations are shown in Table 1.

Table 1: Load case combinations.

Number	Combination	Partial factor of P	Partial factor of W
1	P_1	1.35×1.0	—
2	$P_1 + W_1$	1.2×1.0	1.4×1.0
3	$P_1 + W_2$	1.2×1.0	1.4×1.0
4	$P_1 + W_3$	1.2×1.0	1.4×1.0
5	P_2	1.35×1.0	—
6	$P_2 + W_1$	1.2×1.0	1.4×1.0
7	$P_2 + W_2$	1.2×1.0	1.4×1.0
8	$P_2 + W_3$	1.2×1.0	1.4×1.0
9	P_3	1.35×1.0	—
10	$P_3 + W_1$	1.2×1.0	1.4×1.0
11	$P_3 + W_2$	1.2×1.0	1.4×1.0
12	$P_3 + W_3$	1.2×1.0	1.4×1.0

3. Wind Tunnel Experiment

3.1. Experiment Design. The radio telescope structure has a special form, and the shape factor of the wind load is not in the specification. It is difficult to apply the wind load to the structure. Thus, wind tunnel experiments were used to investigate the wind pressure distribution on the radio telescope reflector.

Accurately reappearing atmospheric boundary flow characteristics are necessary for more reliable experimental results. The passive simulation technology was used to simulate the atmospheric boundary, and wedges, baffles, and rough elements were employed to simulate the landform B, as shown in Figure 5.

The scale model of the telescope is shown in Figure 6. According to the similarity theory,

(a) (b)

Figure 5: Wind experiment: (a) boundary conditions; (b) scale model.

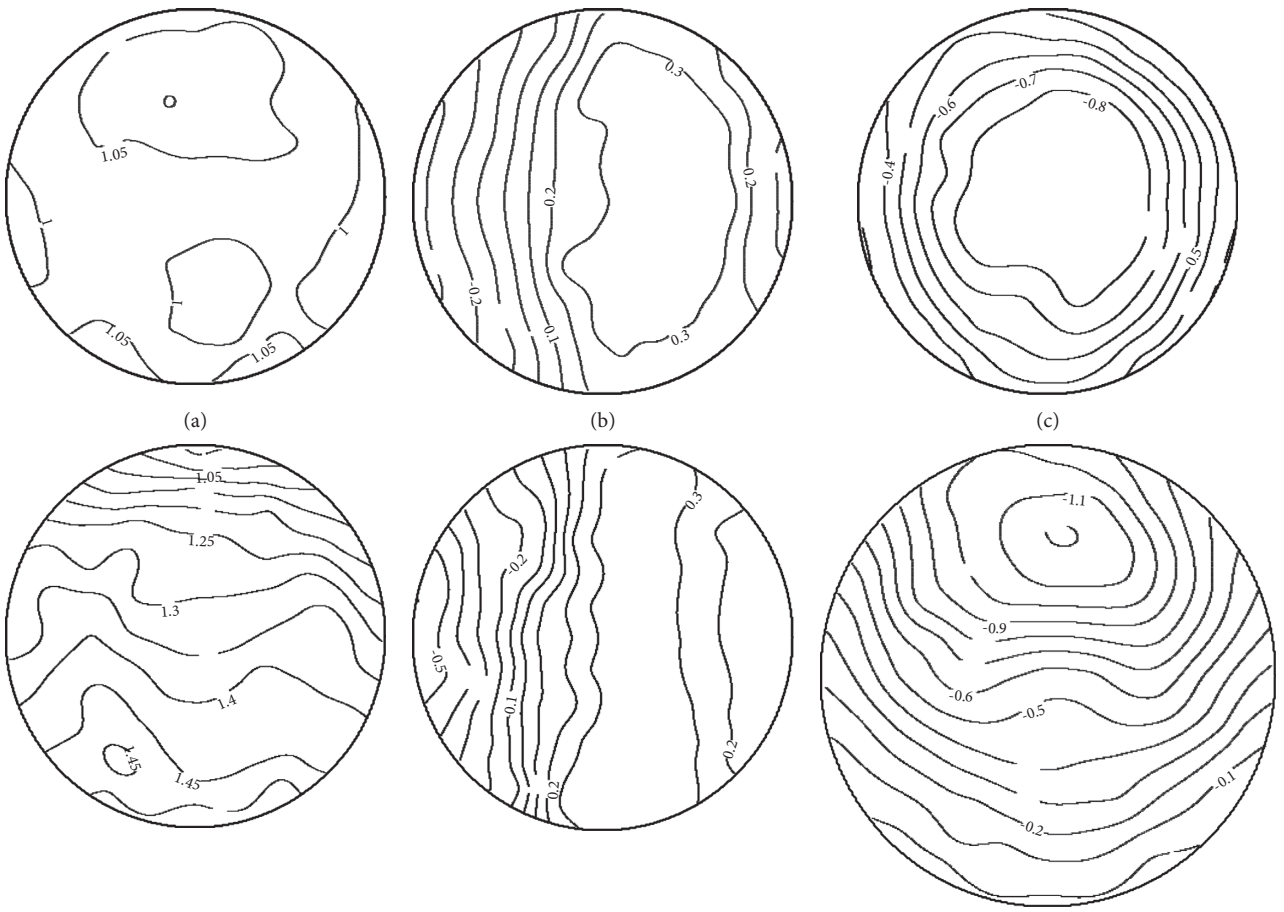

(a) (b) (c)

(d) (e) (f)

Figure 6: Continued.

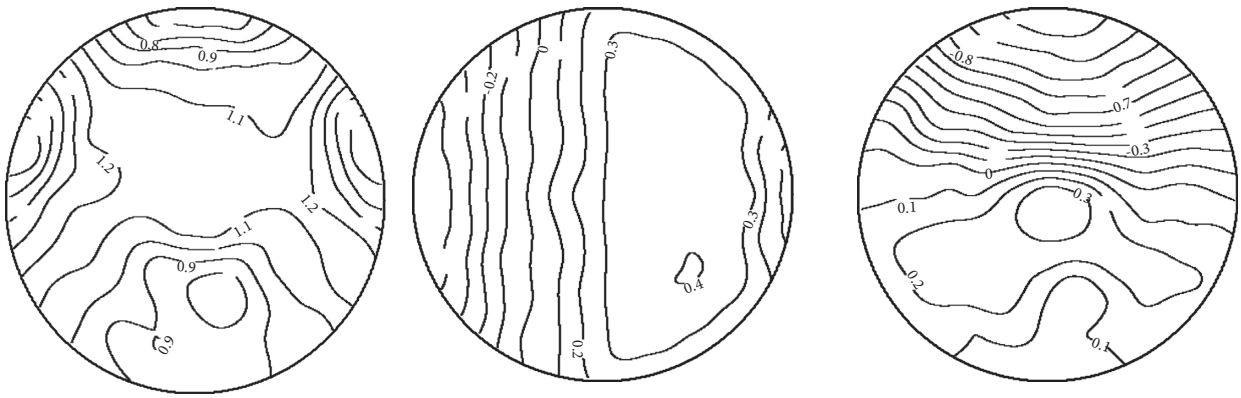

Figure 6: Isolines of wind pressure: (a) pitch angle 5° and wind angle 0°; (b) pitch angle 5° and wind angle 90°; (c) pitch angle 5° and wind angle 180°; (d) pitch angle 30° and wind angle 0°; (e) pitch angle 30° and wind angle 90°; (f) pitch angle 30° and wind angle 180°; (g) pitch angle 60° and wind angle 0°; (h) pitch angle 60° and wind angle 90°; (i) pitch angle 60° and wind angle 180°.

$$\frac{n_m L_m}{U_m} = \frac{n_p L_p}{U_p}, \tag{1}$$

where n is the frequency, L is the geometric dimensioning, U is the wind speed, m denotes the model, and p denotes the prototype.

Limited by the blocking ratio, $L_p/L_m = 110\,\text{m} : 550\,\text{mm} = 1 : 200$. $n_p/n_m = 600\,\text{Hz} : 150\,\text{Hz} = 4 : 1$. $U_p/U_m = 56\,\text{m/s} : 14\,\text{m/s} = 1 : 50$. 91 pressure measuring points were arranged on both convex and concave surfaces of the model. The pressure measuring system is DSM3400.

Before the experiment, the air tightness of the model should be checked first, and then the model with a wind speed of 14 m/s at a pitch angle of 5° and a wind angle of 0° is tested to ensure the reliability of connections and measurements. Subsequently, the experiment and measurement at each pitch angle and wind angle are followed.

3.2. Experiment Results. The collected wind pressure was processed dimensionless according to the following equation:

$$C_{pi}(t) = \frac{(P_i(t) - P_\infty)}{(P_0 - P_\infty)}, \tag{2}$$

where $P_i(t)$ is the wind pressure at measuring point i and P_0 and P_∞ are the average total pressure and average static pressure, respectively. The wind pressure pointing to the reflector is positive, and vice versa.

Figure 6 shows the average wind pressure isolines under different test conditions. When the pitch angle is 5° and the wind angle is 0°, the reflector is completely subjected to positive pressure. When the wind angle is 90°, the negative pressure begins to appear, manifested by wind suction. When the wind angle is 180°, the reflector is completely subjected to negative pressure. The average wind pressure isolines at pitch angles of 30° and 60° are denser than those at the pitch angle of 5°. Specifically, the wind pressure gradient in the edge area changes significantly, while the wind pressure in the central part changes gently.

To obtain the easily applicable wind load, according to the symmetry rule and wind pressure isolines, the reflector is divided from the centre along the circumferential direction and the radial direction. The partitions are shown in Figure 7(a), and the shape factor of wind load according to the following equation is shown in Figure 7(b).

$$\mu_{si} = \overline{C}_{pi}\left(\frac{Z_r}{Z_i}\right)^{2\alpha}, \tag{3}$$

where $\overline{C}_{pi}$ is statistically processed (average) by C_{pi}; α is the roughness index, 0.15; Z_i is the height of measuring point i; and Z_r is the height of reference point.

4. Structural Optimization Method

4.1. Improved Genetic Algorithm. GA consists of chromosome coding, an initial population function, a fitness function, individual crossover, individual replication, individual variation, a penalty function, and other elements. The basic flow is shown in Figure 8.

The optimization variable of the back frame structure is the cross section of robs and cables. There are 16 candidate rob cross sections (Table 2) and 16 candidate prestressed cable cross sections with corresponding prestress (Table 3). All of these are discrete variables, and so the discrete binary coding method is adopted.

There are tens of thousands of robs and cables in the giant radio telescope back frame structure, but there are still hundreds of them even if effectively classified, and each corresponds to more than 20 possible cross sections. Thus, many variables cause great difficulty in the optimization of cross sections. When using the standard GA to optimize the back frame structure, there are so many optimization variables that their number is the same order of magnitude as the population number. This leads to the difference in the initial population being small and not enough. Further, with the individual crossover, replication, and variation, there is a small difference between offspring and parents. It results in the problem of inbreeding and a local minimum value.

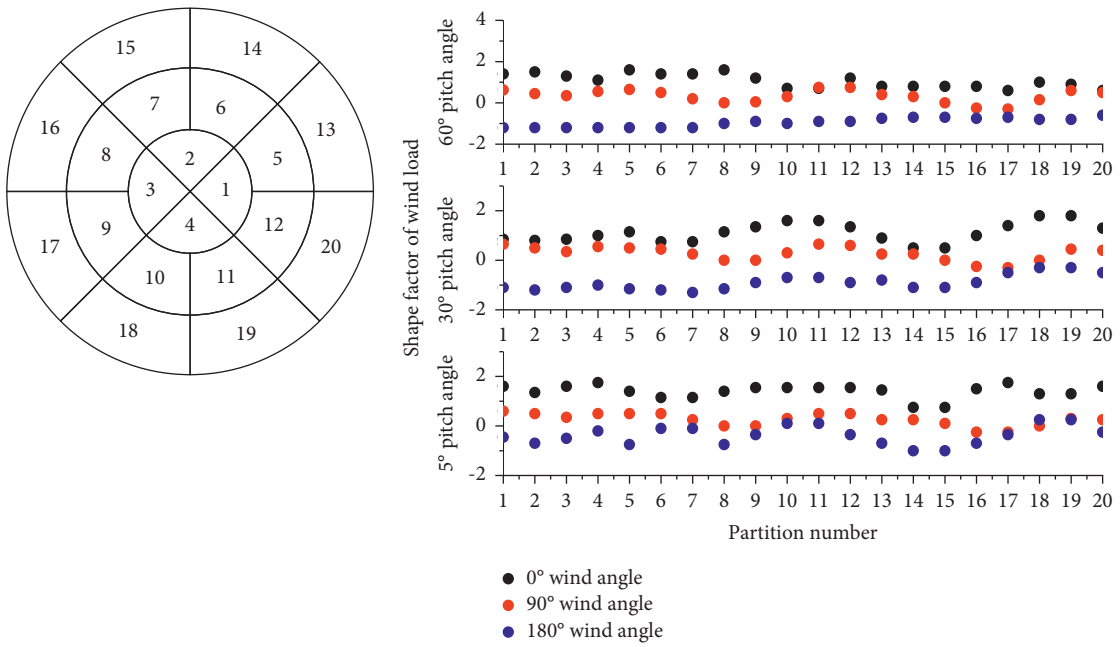

(a) (b)

Figure 7: Wind load: (a) partitions; (b) shape factor.

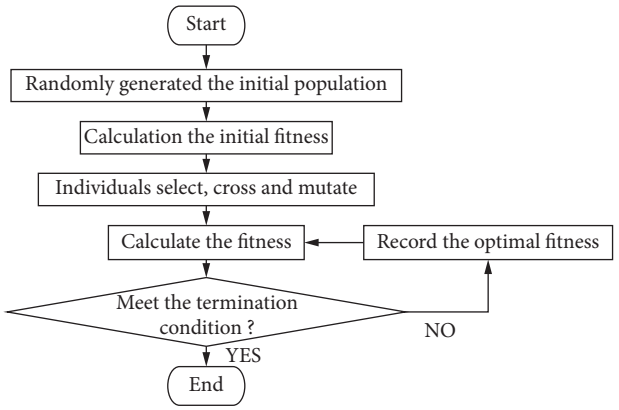

Figure 8: Basic flow of GAs.

Table 2: Rod element data.

Number	Section (mm)
0000	$\varphi 60 \times 3$
0001	$\varphi 70 \times 4$
0010	$\varphi 83 \times 4$
0011	$\varphi 95 \times 4$
0100	$\varphi 102 \times 5$
0101	$\varphi 108 \times 5$
0110	$\varphi 114 \times 5$
0111	$\varphi 121 \times 6$
1000	$\varphi 133 \times 6$
1001	$\varphi 146 \times 7$
1010	$\varphi 159 \times 7$
1011	$\varphi 194 \times 7$
1100	$\varphi 219 \times 8$
1101	$\varphi 245 \times 10$
1110	$\varphi 299 \times 10$
1111	$\varphi 377 \times 16$

Table 3: Cable element data.

Number	Diameter (mm)	Prestress (MPa)
0000	15	600
0001	15	800
0010	15	1000
0011	15	1200
0100	20	600
0101	20	800
0110	20	1000
0111	20	1200
1000	25	600
1001	25	800
1010	25	1000
1011	25	1200
1100	30	600
1101	30	800
1110	30	1000
1111	30	1200

Therefore, to avoid these, the traditional GA should be appropriately improved [40, 41]:

(1) Hamming Distance is used to control the individual differences and to curb the rapid reproduction of individuals. When generating the initial population, it is strictly required that each newly generated individual must be compared with the previous. If the Hamming Distance between the newly generated individual (offspring) and the previously generated individual (parents) is less than a certain preset value, the individual is abandoned and a new individual is generated. This is repeated until the entire initial population is established.

(2) Proportional fitness assignment is the most commonly used selection method in GAs. If only proportional fitness assignment is used for selection, the optimal individual may not be selected and copied to the next generation. Thus, in this sense, the competition between parents and offspring in a selection operator is introduced. Two offspring are generated by two parent individuals. Then, according to the order of respective fitness, two maximal individuals come into the next generation. This can greatly improve the convergence speed of the algorithm.

(3) Because the problem of inbreeding easily occurs in the standard crossover algorithm, it is necessary to improve the crossover operator: crossover points are selected in the effective region to ensure that the newly generated individuals are different from the previous ones. In addition, adaptive crossover probability can be adopted. Low crossover probability is given to individuals whose fitness is higher than the average so that it can be preserved into the next generation, while high crossover probability is given to individuals whose fitness is lower than the average so that they can be eliminated.

4.2. Reflector Accuracy Calculation. In practice, the parabolic reflector cannot completely match the original parabolic reflector, and there are some errors that significantly influence the performance of the radio telescope. There are many reasons for the difference between the reflector and the designed paraboloid. These reasons include the fabrication and installation errors of the reflector panel and deformation caused by various loads, such as the structure weight, the wind load, and the positive and negative temperature differences during operation. Some of these errors are random errors that cannot be optimized. These errors include the fabrication and installation errors of the reflector panel. This study focuses on the optimization of the uneven deformation of the reflector panel that is caused by various loads. The root-mean-square (RMS) of the half optical path difference is the most important index for evaluation of the reflector accuracy. This can be calculated by the following equation:

$$\mathrm{RMS} = \sqrt{\sum \frac{\Delta n_i^2}{N}}, \tag{4}$$

where Δn_i^2 is the normal deviation of point i.

Assuming a new paraboloid, the actual reflector after deformation is matched with the assumed paraboloid. The assumed paraboloid has a relative displacement s and axis rotation with respect to the originally designed paraboloid, and there is a slight change in focal length. There are an infinite number of such assumed paraboloids. However, there is only one that best matches the actual deformed reflector, and this is the best match paraboloid (Figure 9(a)). At this point, the RMS is at a minimum.

Moreover, as shown in Figure 9(b), the actual orifice area of each point on the reflector is not equal because the area of the reflector panel cannot be exactly the same. Furthermore, the orifice area of each point is not equal to the area of the panel to which the point belongs. Instead, it is equal to the projected area of the panel to which the point belongs. The difference between the two areas must be taken into account in the calculation. In this paper, equation (4) is modified to obtain the following equation:

$$\mathrm{RMS} = \sqrt{\sum \frac{\Delta n_i^2 \times \Delta A_i}{A}}, \tag{5}$$

where ΔA_i is the modified area of the reflector panel and A is the total area of reflector.

5. Optimization of the 110 m Aperture Radio Telescope Back Frame Structure

In this chapter, the improved GA, described in the third chapter, is used for the optimization design and calculation of the new prestressed back frame structure. The specific contents are as follows:

(1) Optimizing the new prestressed back frame structure with the goal of improving the reflector accuracy and reducing the weight

(2) Checking the strength of the new prestressed back frame structure under static conditions according to the specifications

(3) Analysing the seismic responses of the new prestressed back frame structure in earthquakes according to the specifications

Different elements are used for simulation in analysis. Tables 4 and 5 show the used finite element elements and material properties, respectively.

5.1. Accuracy and Weight Control. When the reflector is installed, the angle is 45° and the RMS is 0. When evaluating the reflector accuracy, pitch angles of 0° and 90° are selected in this paper. The deformation of each back frame structure scheme is shown in Figures 10 and 11. The accuracy and weight comparison are shown in Table 6.

A pitch angle of 0° refers to a flat state, and the maximum deformation of the traditional scheme is 177 mm. The deformation of three new prestressed back frame structure schemes is not different from that of the traditional scheme, and the maximum deformation is slightly reduced to 174 mm, 174 mm, and 170 mm, respectively. In this state, the prestressed back frame structure can reduce the structural deformation to some extent, but the reduction is not large.

A pitch angle of 90° refers to the state pointing to the sky, and the maximum deformation of each scheme is about 40 mm. The minimum deformation of the traditional rod system is in the innermost circle, and the deformation gradually increases from this innermost circle to the outside. The minimum deformation of the prestressed back frame structure schemes appears in the middle part and gradually increases from the middle part to both sides. The deformation state of the prestressed back frame structure is obviously different from that of the traditional rod system.

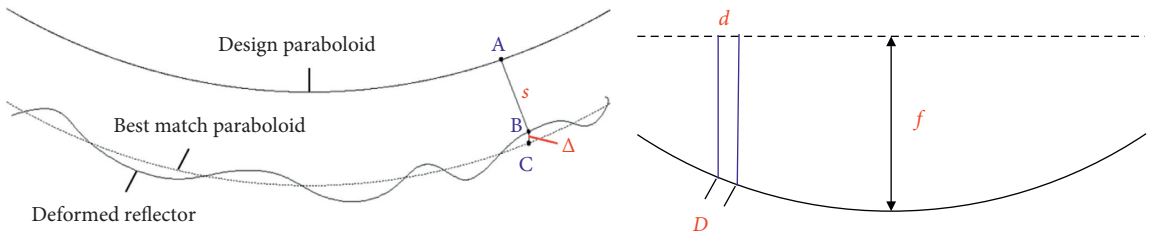

Figure 9: The difference between the reflector and the designed paraboloid: (a) deviation to the best match paraboloid; (b) area projection.

Table 4: Finite element elements used in analysis.

Part	Element
Back frame	Pipe16
Pitching device, azimuth mount, actuators	Beam4
Reflector	Shell181

Table 5: Material properties.

Material properties	Steel	Aluminium
Elasticity modulus (N/m^2)	2.06×10^{11}	0.7×10^{11}
Poisson's ratio	0.30	0.33
Density (kg/m^3)	7850	2700

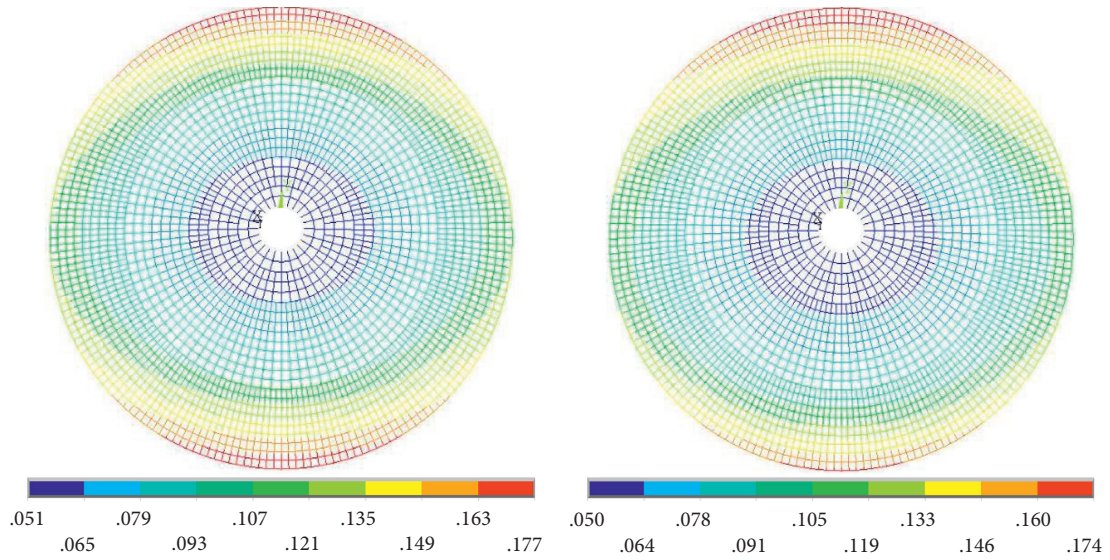

Figure 10: Continued.

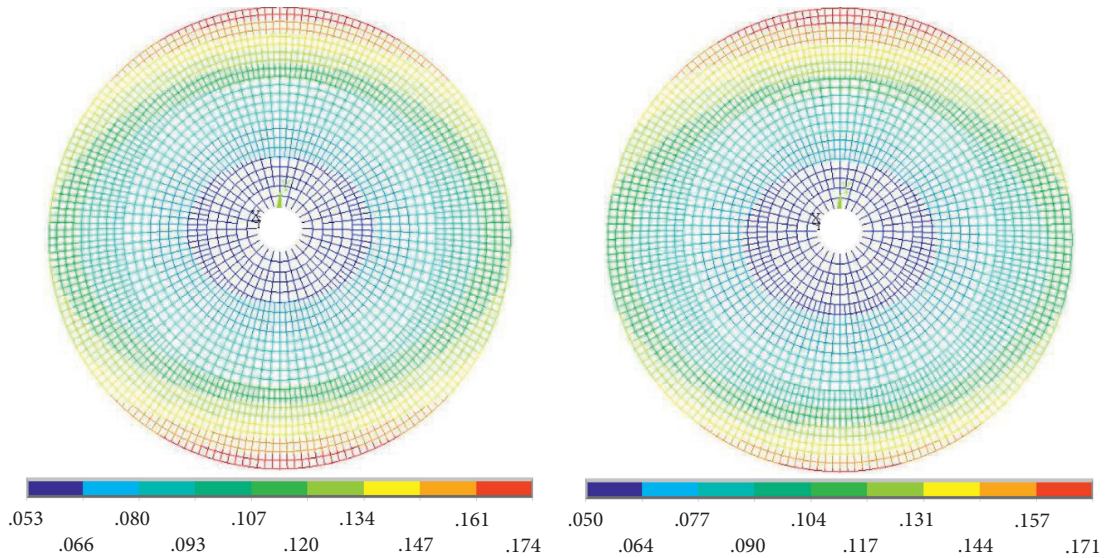

(c) (d)

Figure 10: Deformation of the back frame structure in pitch angle 0°: (a) rod system; (b) scheme 1; (c) scheme 2; (d) scheme 3.

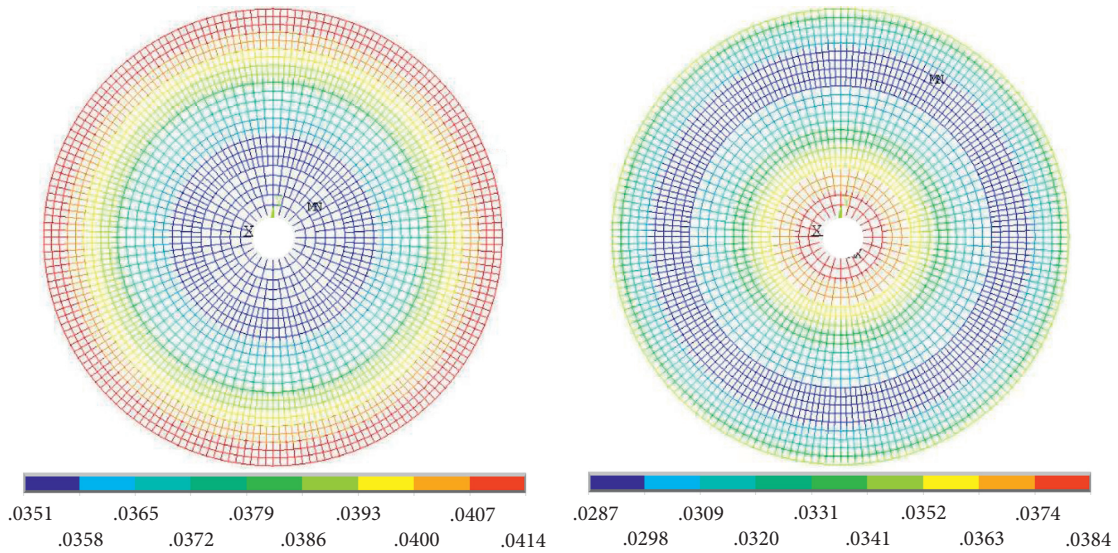

(a) (b)

Figure 11: Continued.

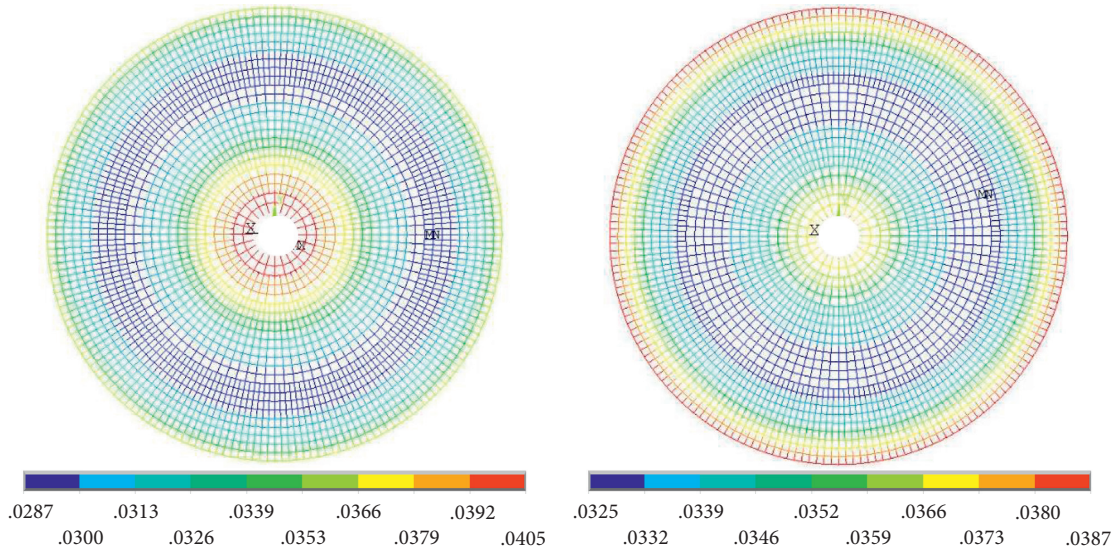

(c) (d)

Figure 11: Deformation of the back frame structure in pitch angle 90°: (a) rod system; (b) scheme 1; (c) scheme 2; (d) scheme 3.

Table 6: Scheme comparison of back frame structure.

Index	Traditional scheme	Scheme 1	Scheme 2	Scheme 3
Weight (t)	1095	1050	1108	1084
RMS (mm)	0.198	0.180	0.162	0.161

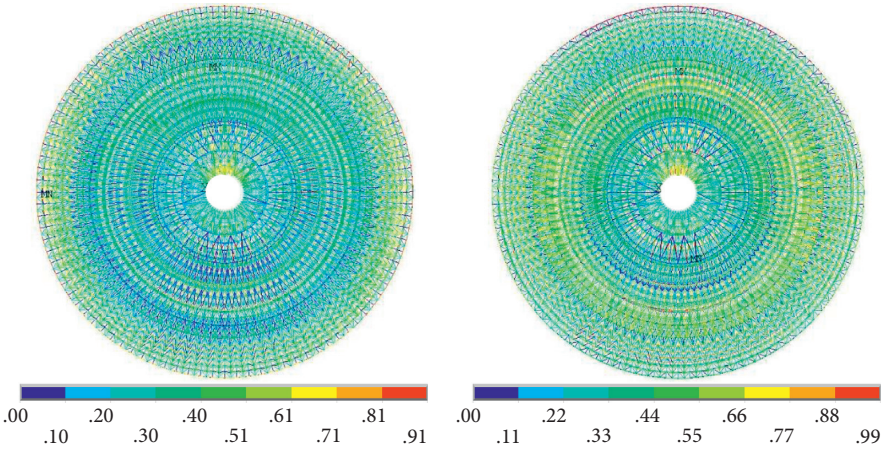

(a) (b)

Figure 12: Continued.

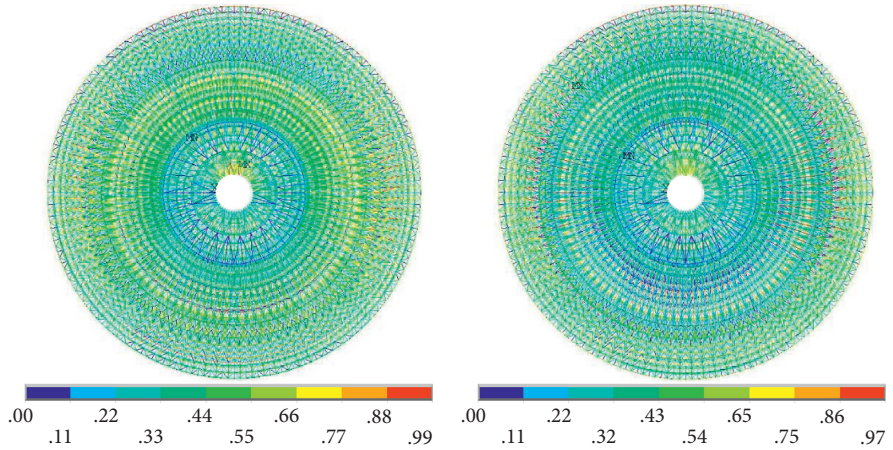

(c) (d)

Figure 12: Stress ratio of the back frame structure: (a) rod system; (b) scheme 1; (c) scheme 2; (d) scheme 3.

Table 7: Seismic action calculation parameters.

Calculation parameters		Value
Material properties	Frequent earthquakes	Isotropic linear elastic material
	Rare earthquakes	Bilinear model, the elastic modulus changes to 2% of the initial elastic modulus after yielding
Damping ratio		0.02
Seismic action		3D, peak acceleration $a_x : a_y : a_z = 1.0 : 0.85 : 0.65$
Design intensity		8 ($\alpha = 0.20$ g)
Site classification for construction		II
Period		Basic frequency: 0.656 Hz, basic period: 1.52 s

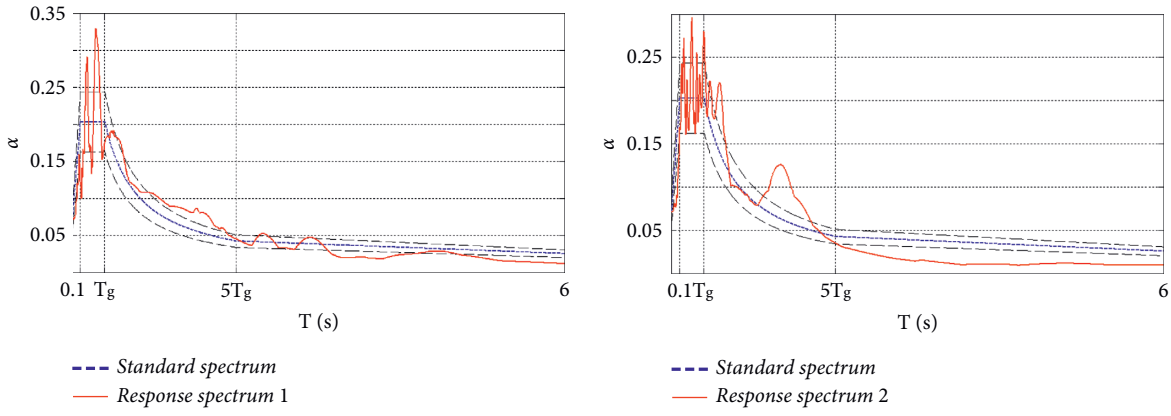

(a) (b)

Figure 13: Continued.

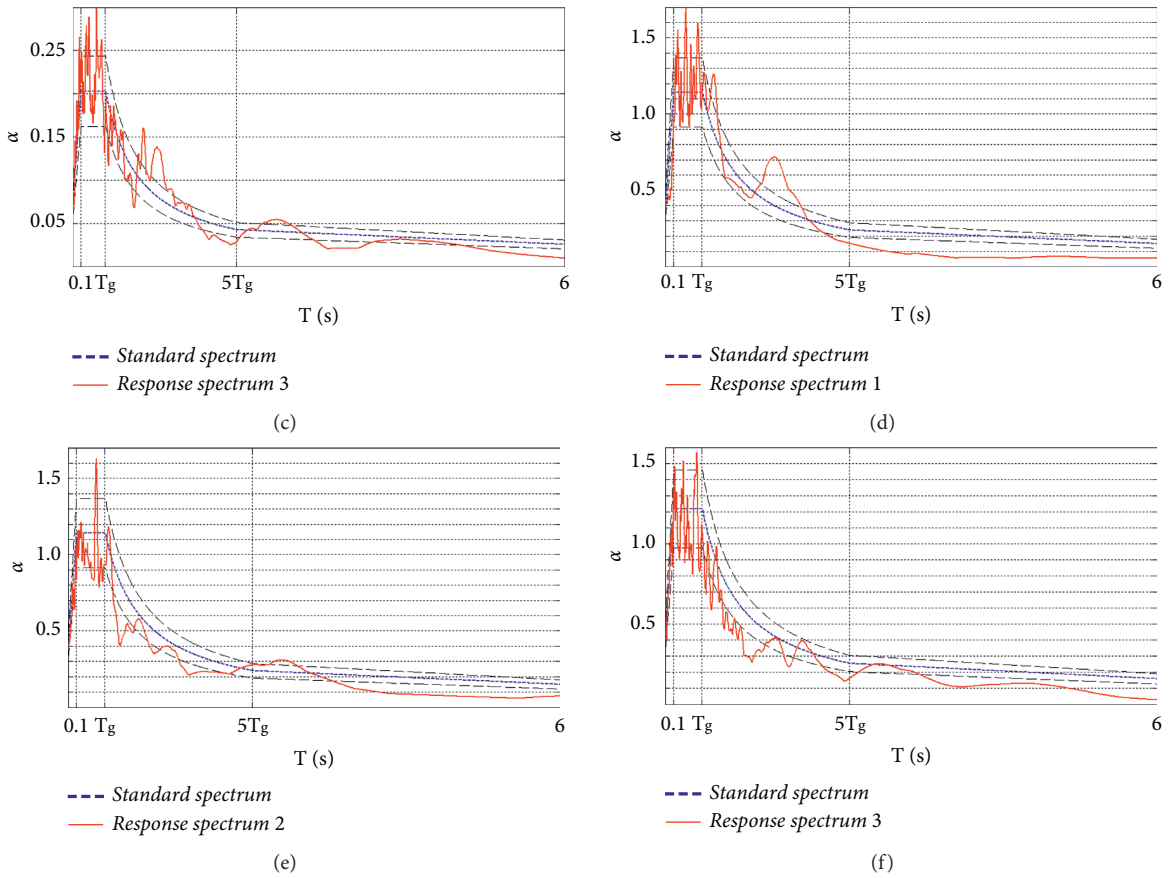

Figure 13: Seismic response spectra: (a) frequent earthquake: response spectrum 1; (b) frequent earthquake: response spectrum 2; (c) frequent earthquake: response spectrum 3; (d) rare earthquake: response spectrum 1; (e) rare earthquake: response spectrum 2; (f) rare earthquake: response spectrum 3.

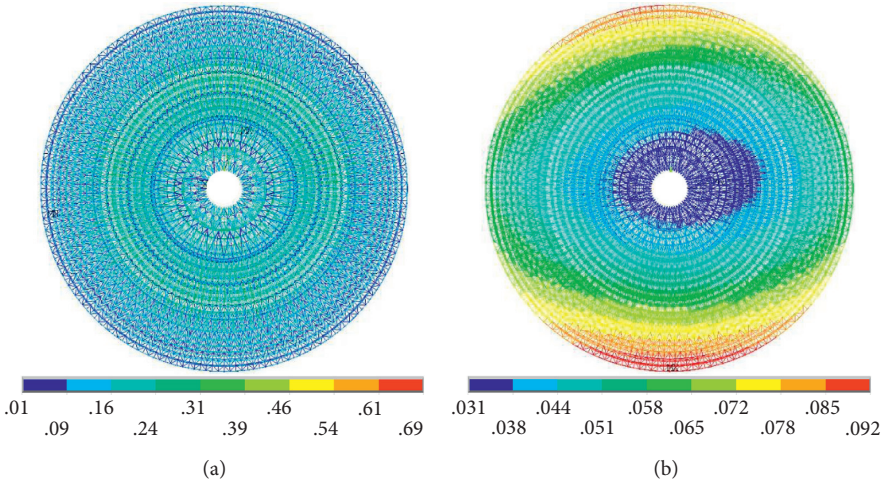

Figure 14: Time history analysis results in frequent earthquakes: (a) envelope diagram of displacement; (b) envelope diagram of stress ratio.

Specifically, the deformation is less than that of the traditional scheme. Therefore, the introduction of prestressed cables can change the stress state of the structure. The structural stiffness increases, and the deformation decreases.

After the traditional rod system is optimized, the reflector accuracy RMS is 0.198 mm, and the structure weight is 1095 t. Among the three new prestressed back frame structures, the optimal reflector accuracy appears in Scheme

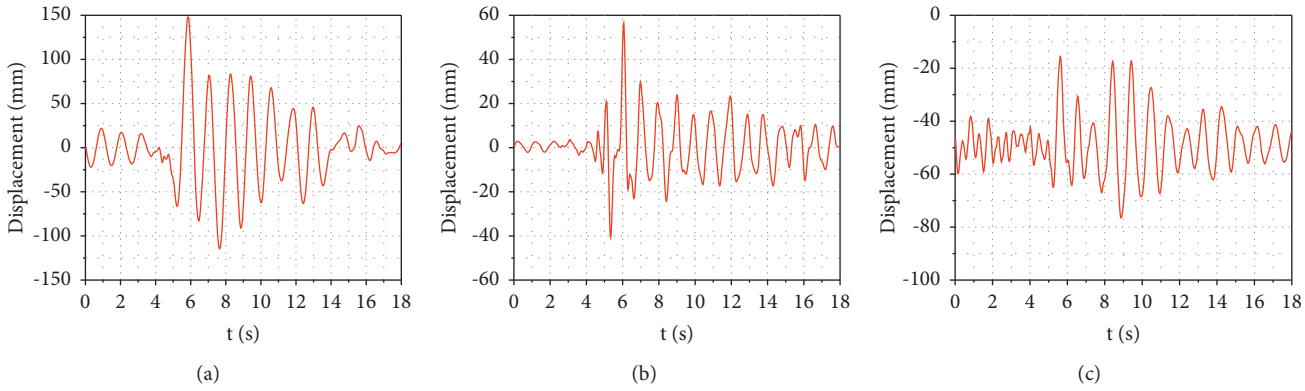

Figure 15: Time history curve of the maximum displacement point: (a) x direction; (b) y direction; (c) z direction.

3, reaching the value of 0.161 mm. The accuracy is improved by about 20% compared with the traditional scheme, and the weight is also slightly reduced.

5.2. Strength Check. The load of each test condition in Section 2.2 is applied to the structure. The load is combined, and then the structural strength is checked according to the specifications. The maximum stress ratio under different test conditions is extracted and plotted in a nephogram (Figure 12). The strength of the four kinds of the back frame structures meets the requirements.

5.3. Seismic Response Analysis. Furthermore, the seismic responses of the 110 m aperture radio telescope prestressed back frame structure in earthquakes are analysed. The time history analysis method is used for calculations. The corresponding calculation parameters are shown in Table 7. According to the specifications, two actual response spectra, recorded by strong earthquakes, and one artificial simulated response spectrum are selected for time history analysis [42]. The final selected seismic response spectra are shown in Figure 13.

Combining frequent earthquakes with static conditions in Table 1, the partial coefficient and combination coefficient of the constant load are changed to 1.2×1.0, those of the seismic load are 1.3×1.0, and those of the wind load are 1.4×0.2. Figure 14 shows the structural displacement response envelope diagram and stress ratio nephogram calculated by three frequent earthquake response spectra. Within these frequent earthquakes, the maximum displacement of the back frame structure is 92 mm, and the overall displacement is small. The maximum stress ratio is 0.69, and the stress of most rods is low. Thus, the structure has a high safety degree, and the strength meets the requirements of the specification.

Figure 15 shows three directional time history curves of the maximum displacement point of the back frame structure under rare earthquakes. As seen from the figure, all of the time history curves converge. In addition, Table 8 shows the percentage of robs that become plastic under rare earthquakes. Only a small number of the robs become plastic, and the structure is basically in an elastic state, which meets the seismic fortification requirements.

Table 8: Statistics of plastic robs in rare earthquakes.

Response spectrum	Number of plastic robs	Proportion (%)
1	60	0.22
2	45	0.16
3	62	0.22

6. Conclusions

This study proposed a prestressed radio telescope back frame structure scheme. The improved GA is used to optimize the 110 m aperture radio telescope back frame structure. The prestressed back frame structure provides a technical reserve for the design and construction of the 110 m aperture radio telescope. The main contributions can be summarized as follows:

(1) A new structural design scheme for applying prestressed cables to the back frame structure is proposed to improve the reflector accuracy and reduce the weight of the structure.

(2) Wind tunnel experiments are used to investigate the wind pressure distribution on the telescope reflector and obtain the average wind pressure isolines under different test conditions. The experimental data are also translated into easily applied wind load.

(3) The standard GA is improved and modified for addressing computational complexity so that it can be used to optimize the cross section of robs and cables of the back frame structure.

(4) The improved GA is used to optimize the prestressed back frame structure. Compared with the traditional rod system, the three schemes with prestressed cable have smaller maximum deformation and higher reflector accuracy. The accuracy increases by 20%, and the weight is slightly reduced.

(5) The strength of the back frame structure is checked. The stress of most robs is low, so the structure has a high safety degree. Moreover, the structure meets the

seismic fortification requirements both in frequent and rare earthquakes.

For the optimization of the 110 m aperture radio telescope prestressed back frame structure, the weight of the structure is not significantly reduced. The reason for this is that the cross section of the rods cannot be reduced any further because of the limit of the slenderness ratio. Future research should focus on reducing the structure weight as much as possible using other feasible approaches.

Data Availability

All data used to support the findings of this study are available from the corresponding author upon request.

Conflicts of Interest

The authors declare that they have no conflicts of interest.

References

[1] Y. Qiu, Q. Xu, J. Tian, and Q. Liu, "On the interference characteristics of fully steerable radio telescope," *SCIENTIA SINICA Physica, Mechanica & Astronomica*, vol. 47, pp. 99–107, 2017.

[2] M. Losacco and L. Schirru, "Orbit determination of resident space objects using the P-band mono-beam receiver of the sardinia radio telescope," *Applied Sciences*, vol. 9, no. 19, Article ID 4092, 2019.

[3] G. Kazezkhan, B. Xiang, N. Wang, and A. Yusup, "Dynamic modeling of the stewart platform for the NanShan radio telescope," *Advances in Mechanical Engineering*, vol. 12, no. 7, Article ID 168781402094007, 2020.

[4] R. Nan and B. Peng, "A Chinese concept for the 1 km^2 radio telescope," *Acta Astronautica*, vol. 46, no. 10–12, pp. 667–675, 2000.

[5] B. Zhu, L. Qian, and Y. Yue, "The conceptual designs of radio telescopes in Guizhou karst region," *SCIENTIA SINICA Physica, Mechanica & Astronomica*, vol. 50, Article ID 089501, 2020.

[6] Y. Qiu, "A novel design for giant radio telescopes with an active spherical main reflector," *Chinese Astronomy and Astrophysics*, vol. 22, no. 3, pp. 361–368, 1998.

[7] Y. Liu and E. Dai, "Structural selection and accuracy control of the large aperture fully steerable antenna," *The Structural Design of Tall and Special Buildings*, vol. 27, no. 11, Article ID e1482, 2018.

[8] R. M. Prestage, K. T. Constantikes, T. R. Hunter et al., "The green bank telescope," *Proceedings of the IEEE*, vol. 97, no. 8, pp. 1382–1390, 2009.

[9] R. Wielebinski, N. Junkes, and B. H. Grahl, "The Effelsberg 100-m radio telescope: construction and forty years of radio astronomy," *Journal of Astronomical History and Heritage*, vol. 14, no. 1, pp. 3–21, 2011.

[10] S. Von Hoerner, "Design of large steerable antennas," *The Astronomical Journal*, vol. 72, pp. 35–47, 1967.

[11] C. Fleury, "Structural weight optimization by dual methods of convex programming," *International Journal for Numerical Methods in Engineering*, vol. 14, no. 12, pp. 1761–1783, 1979.

[12] G. Sander and C. Fleury, "A mixed method in structural optimization," *International Journal for Numerical Methods in Engineering*, vol. 13, no. 2, pp. 385–404, 1978.

[13] C. Fleury, "An efficient optimality criteria approach to the minimum weight design of elastic structures," *Computers & Structures*, vol. 11, no. 3, pp. 163–173, 1980.

[14] S. von Hoerner, "Homologous deformations of tiltable telescope," *Journal of Structural Engineering*, vol. 93, pp. 1305–1325, 1967.

[15] S. Chen and S. Ye, "Homogenous design for modified curved antennas," *Journal of Xidian University*, vol. 1, pp. 3–11, 1981.

[16] R. Levy and R. Melosh, "Computer design of antenna reflectors," *Journal of the Structural Division*, vol. 99, no. 11, pp. 2269–2285, 1973.

[17] H. Dehghani, I. Mansouri, A. Farzampour, and J. W. Hu, "Improved homotopy perturbation method for geometrically nonlinear analysis of space trusses," *Applied Sciences*, vol. 10, no. 8, Article ID 2987, 2020.

[18] S. O. Degertekin, L. Lamberti, and I. B. Ugur, "Sizing, layout and topology design optimization of truss structures using the Jaya algorithm," *Applied Soft Computing*, vol. 70, pp. 903–928, 2018.

[19] S. O. Degertekin, L. Lamberti, and I. B. Ugur, "Discrete sizing/layout/topology optimization of truss structures with an advanced Jaya algorithm," *Applied Soft Computing*, vol. 79, pp. 363–390, 2019.

[20] N. Cui, S. Huang, and X. Ding, "An improved strategy for genetic evolutionary structural optimization," *Advances in Civil Engineering*, vol. 2020, Article ID 5924198, 2020.

[21] B. San, Z. Xiao, and Y. Qiu, "Simultaneous shape and stacking sequence optimization of laminated composite free-form shells using multi-island genetic algorithm," *Advances in Civil Engineering*, vol. 2019, Article ID 2056460, 2019.

[22] N.-I. Kim, Y.-W. Kim, J. Lee, and J.-W. Kang, "Two-stage optimization based on force method for damage identification of planar and space trusses," *International Journal of Steel Structures*, vol. 18, no. 1, pp. 1–12, 2018.

[23] W. He and Y. Shi, "Multiobjective construction optimization model based on quantum genetic algorithm," *Advances in Civil Engineering*, vol. 2019, Article ID 5153082, 2019.

[24] D. E. Goldberg and M. Samtani, "Engineering optimization via genetic algorithms," in *Proceedings of the 9th Conference on Electronic Computations*, pp. 471–482, ASCE, New York, NY, USA, 1986.

[25] S. Rajeev and C. S. Krishnamoorthy, "Discrete optimization of structures using genetic algorithms," *Journal of Structural Engineering*, vol. 118, no. 5, pp. 1233–1250, 1992.

[26] H. Adeli and N. T. Cheng, "Integrated genetic algorithm for optimization of space structures," *Journal of Aerospace Engineering*, vol. 6, no. 4, pp. 315–328, 1993.

[27] M. B. Prendes Gero, A. Bello García, and J. J. del Coz Díaz, "A modified elitist genetic algorithm applied to the design optimization of complex steel structures," *Journal of Constructional Steel Research*, vol. 61, no. 2, pp. 265–280, 2005.

[28] M. B. Prendes Gero, A. B. García, and J. J. del Coz Díaz, "Design optimization of 3D steel structures: genetic algorithms vs. classical techniques," *Journal of Constructional Steel Research*, vol. 62, no. 12, pp. 1303–1309, 2006.

[29] T. Stanković, M. Štorga, and D. Marjanović, "Synthesis of truss structure designs by NSGA-II and NodeSort algorithm," *Strojniski Vestnik*, vol. 58, no. 3, pp. 203–212, 2012.

[30] M. Kociecki and H. Adeli, "Two-phase genetic algorithm for size optimization of free-form steel space-frame roof structures," *Journal of Constructional Steel Research*, vol. 90, no. 9, pp. 283–296, 2013.

[31] K. Grygierek, "Optimization of trusses with self-adaptive approach in genetic algorithms," *Architecture Civil Engineering Environment*, vol. 9, no. 4, p. 1, 2016.

[32] H. Assimi and A. Jamali, "A hybrid algorithm coupling genetic programming and Nelder-Mead for topology and size optimization of trusses with static and dynamic constraints," *Expert Systems with Applications*, vol. 95, pp. 127–141, 2018.
[33] I. Delyová, P. Frankovský, J. Bocko et al., "Sizing and topology optimization of trusses using genetic algorithm," *Materials*, vol. 14, no. 4, Article ID 715, 2021.
[34] J. D. Villalba-Morales and S. Ramirez-Echeverry, "An approximation to the use of self-adaptive genetic algorithms in weight optimization of 3-D steel trusses," *Ingenieria Y Competitividad*, vol. 23, p. 1, 2021.
[35] Y. Ren, Z. Zhu, Z. Fan, and Q. Huang, "Estimation of extreme cable forces of cable-stayed bridges based on monitoring data and random vehicle models," *Advances in Civil Engineering*, vol. 2021, Article ID 8897427, 15 pages, 2021.
[36] X. X. Cheng, F. B. Ma, J. Q. Chen, B. Dong, and G. Wu, "Bearing repair and monitoring for poyanghu cable-stayed bridge," *Advances in Civil Engineering*, vol. 2020, Article ID 8819360, 15 pages, 2020.
[37] Y. Ruan, B. Luo, M. Ding, L. Huang, and Z. Guo, "Theoretical and experimental study on the antisliding performance of casting steel cable clamps," *Advances in Civil Engineering*, vol. 2019, Article ID 1438754, 18 pages, 2019.
[38] R. Nie, B. He, S. Yan, and X. Ma, "Optimization design method for the cable network of mesh reflector antennas considering space thermal effects," *Aerospace Science and Technology*, vol. 94, Article ID 105380, 2019.
[39] G. Yang, D. Yang, Y. Zhang, and J. Du, "Form-finding design of cable-mesh reflector antennas with minimal length configuration," *Aerospace Science and Technology*, vol. 63, pp. 9–17, 2017.
[40] M. Kaya, "The effects of a new selection operator on the performance of a genetic algorithm," *Applied Mathematics and Computation*, vol. 217, no. 19, pp. 7669–7678, 2011.
[41] T. Qiu, H. Hu, R. Chen, Q. Zhou, Q. Guan, and X. Li, "A multi-root solver for discontinuous and non-differentiable equations by integrating genetic algorithm and derivative-free iterative methods," *Applied Soft Computing*, vol. 109, Article ID 107493, 2021.
[42] China Academy of Building Research, *Code for Seismic Design of Buildings*, GB50011-2010, China, 2016.